







Skin-adhesive stretchable conductors for wireless vital diagnostics

Taeyeon Oh^{a,1}, Minwoo Song^{b,1}, Hyunkeun Lee^{c,1} , Hansu Kim^a, Hyeongbeom Lee^a, Yong-Ryun Jo^d, Tae-Wook Kim^e , Gui Won Hwang^b, Jinhyung Kim^b, Jihun Son^b, Chanhyeok Park^c, Hanbit Jin^f, Chan-Hwa Hong^f, Inho Lee^a, Jun-Gyu Choi^g, Ji Hwan Kim^h, Alexander Tipan-Quishpeⁱ , Myung-Han Yoonⁱ, Hye Jin Kim^{f,*}, Changhyun Pang^{b,j,**}, Sungjun Park^{a,g,***} 

^a Department of Intelligence Semiconductor, Ajou University, Suwon, Gyeonggi-do 16499, Republic of Korea

^b School of Chemical Engineering, Sungkyunkwan University (SKKU), 2066 Seobu-ro, Jangan-gu, Suwon 16419, Republic of Korea

^c Department of AI Semiconductor Engineering, Korea University Sejong Campus, 2511 Sejong-ro, Sejong 30019, Republic of Korea

^d GIST Advanced Institute of Instrumental Analysis (GAIA), Electron Microscopy Laboratory, Gwangju Institute of Science and Technology, Gwangju 61005, Republic of Korea

^e Department of Flexible and Printable Electronics, Jeonbuk National University, Jeonju, Jeonbuk 54896, Republic of Korea

^f Electronics and Telecommunications Research Institute (ETRI), Daejeon 34129, Republic of Korea

^g Department of Electrical and Computer Engineering, Ajou University, Suwon 16499, Republic of Korea

^h Department of Materials Science and Engineering, Seoul National University, Seoul 08826, Republic of Korea

ⁱ School of Materials Science and Engineering, Gwangju Institute of Science and Technology (GIST), 123 Cheomdangwagi-Ro, Buk-Gu, Gwangju 61005, Republic of Korea

^j Samsung Advanced Institute for Health Science & Technology (SAIHST), Sungkyunkwan University (SKKU), 2066 Seobu-ro, Jangan-gu, Suwon 16419, Republic of Korea

ARTICLE INFO

Keywords:

Stretchable conductor
Robust conductive path
Bioinspired adhesive structure
Monolithically integration
Wearable diagnostics monitoring system

ABSTRACT

Continuous physiological signal monitoring and diagnosis are crucial for proactive health management and timely interventions. Key challenges include achieving non-toxic adhesion of stretchable conductors to dynamic skin and integration with lightweight, wearable circuits equipped diagnosing algorithms. We propose wireless physiological monitoring with vital diagnosis, featuring octopus-inspired micromembrane structure electrodes that enhance both adhesion and permeability. These stretchable electrodes exhibit a conductivity of over 2700 S/cm and maintain stretchability up to 1000 %, with minimal degradation after 1000 cycles of deformation. Adhesion reaches 12 kPa, ensuring durability for over 1000 attachment-detachment cycles and long-term attachment exceeding 24 h without skin toxicity. The system, connected to a miniaturized wireless circuit (2.8 g), facilitates real-time, accurate collection of electrocardiography (ECG), electromyography (EMG), electrooculography (EOG), and electroencephalography (EEG) signals. As proof of concept, ECG signals from real subjects processed with a transfer-learning algorithm achieved over 93.3 % diagnostic accuracy, paving the way for reliable, personalized health monitoring.

1. Introduction

Monitoring and diagnosing long-term physiological signals have gained significant attention over the past decade due to their ability to deliver real-time health insights [1–5]. Continuous monitoring is

essential, as abnormal physiological signals often occur intermittently rather than periodically, requiring long-term data collection for accurate detection. This capability enables prompt intervention and optimized treatment when such irregular health indicators are identified based on extended measurements [6,7]. To ensure the robust performance of

* Corresponding author.

** Corresponding author at: School of Chemical Engineering, Sungkyunkwan University (SKKU), 2066 Seobu-ro, Jangan-gu, Suwon 16419, Republic of Korea.

*** Corresponding author at: Department of Intelligence Semiconductor, Ajou University, Suwon, Gyeonggi-do 16499, Republic of Korea.

E-mail addresses: nolawara@etri.re.kr (H.J. Kim), chpang@skku.edu (C. Pang), sj0223park@ajou.ac.kr (S. Park).

¹ These authors contributed equally to this work.

wearable health monitoring devices, key factors of the bio-interface—particularly the electrode in direct contact with the skin—must be carefully optimized: (1) High conductivity for low-noise, accurate physiological signals measurement. (2) Stretchability under high strain, achieved by developing conductive pathways with strong mechanical tolerance, allowing for freedom in body movement and electrode positioning. (3) Tight adhesion to complex skin topographies, facilitated by materials with high adhesive properties, ensuring a stable, smooth connection to various skin textures without bending or fracture, enabling consistent physiological signal measurement. (4) Biocompatibility, including non-toxicity and the prevention of irritation or rashes, allowing for long-term comfortable adhesion. (5) Integration of flexible and lightweight circuits with efficient algorithms and wireless data transmission technology while ensuring accurate disease diagnosis.

State-of-the-art stretchable conductors have made significant advancements, achieving impressive stretchability up to 500 % and high conductivity values of 15,000 S/cm [8]. These advancements are attributed to the innovative use of intrinsically stretchable polymer embedded with conducting materials, such as conducting polymers [9, 10], liquid metals [11,12], and metal nanoparticles [13,14]. Additionally, conformal and strong adhesion of the electrode to the skin through hydrogen bonding demonstrated impressive performance, achieving an adhesion strength of 7.36 kPa, stretchability of 50 %, and conductivity of 400 S/cm, showcasing superior adhesion properties [15,16]. Despite these advancements, adhesion stability remains a critical limitation. Sweat and dust on the skin can inhibit conformal contact between the material and the skin surface, compromising long-term performance.

It remains challenging to achieve and maintain low impedance, strong adhesiveness, and stretchability at the skin interface for epidermal electrodes. This underscores the need for developing durable, semi-permanent electrode materials that can be repeatedly applied without compromising performance. The primary difficulty lies in the properties of intrinsically conductive materials, such as metal flakes, nanoparticles, and liquid metals, whose high surface tension limits uniform dispersion, resulting in phase separation within complex matrices [17,18]. Liquid metals, in particular, tend to undergo surface oxidation when exposed to air, which reduces their stability, flexibility, and conductivity [19,20], making them unsuitable for prolonged use. Chemical adhesives can further complicate this issue by disrupting smooth charge transport along the conductive path under mechanical deformation and leaving residues on the skin [21], which hinders repeated use [22]. This trade-off between low skin-electrode impedance and reliable adhesion underscores the necessity of developing integrated material systems that balance electrical and mechanical performance with skin conformity. Therefore, overcoming this challenge requires developing materials with optimized compositions and designing structures that ensure effective skin application, integrating them monolithically. Seamlessly integrating the conductivity secured through the conductor with adhesion of the adhesive structure in the fabricated electrode will enhance the practicality and durability of epidermal applications.

This paper proposes a long-term, wireless physiological monitoring platform that integrates machine learning with a mechanically robust, stretchable conductor and a bioinspired adhesive structure. The stretchable conductor developed through the optimization of organic-inorganic hybrid composites achieved high conductivity (>2700 S/cm) and elasticity (>1000 %). The robust conductive path, which incorporates Ag nanoparticles (Ag NPs), effectively distributes stress under significant deformation, demonstrating excellent mechanical durability. After 1000 cycles of repetitive deformation and 200 % tensile strain, the change in resistance was negligible, enabling the establishment of a scalable monitoring system for personalized applications. For long-term physiological signal monitoring, adhesive electrodes were developed using octopus suckers inspired micromembrane architecture (OIA) interlocked with a stretchable conductor. These skin-compatible electrodes demonstrated excellent physical skin adhesion (~ 12 kPa)

and low electrical impedance ($8.9 \times 10^5 \Omega \text{ cm}^2$ at 1 Hz), comparable to that of commercially available electrodes. Additionally, they maintained minimal changes in adhesive strength after 1000 cycles of repeated attachment and proved non-toxic to the skin even after 24 h of continuous use. The adhesive electrodes are integrated with a lightweight (2.8 g) flexible printed circuit board (FPCB) to collect physiological signals, wirelessly transmit them to a mobile device, and analyze the data for disease classification. Based on physiological signals measured from 15 healthy individuals, the lightweight 11.7 g system classified diseases with over 93.3 % accuracy, demonstrating promising potential in smart disease diagnosis and treatment. This advancement will be instrumental in developing future long-term, longitudinal, and personalized wearable health monitoring systems.

2. Design of wireless vital diagnostics and skin-compatible stretchable conductors

Fig. 1a presents a schematic of the wireless vital-diagnostic system. (i) Stretchable conductors offer stable interconnections and versatile positioning on the body. It was optimized through sophisticated composition engineering of Ag flakes, poly(3,4-ethylenedioxythiophene) polystyrene sulfonate (PEDOT:PSS), an ionic liquid (IL) (1-Ethyl-3-methylimidazolium bis (trifluoromethylsulfonyl) imide (EMIM TFSI)), waterborne polyurethane (WPU), and additives—achieving both exceptional conductivity > 2700 S/cm and stretchability >1000 %, simultaneously. The conductive pathway remained stable under significant deformation and repeated stretching. This demonstrates that the stretchable conductor can serve as a flexible interconnection between the adhesive electrode and the wireless ECG module. The robust conductor network enables a personalized vital-monitoring system where electrodes can be positioned according to individual body size. (ii) A skin-adhesive electrode was designed using an OIA monolithically interlocked with a stretchable conductor, enabling precise physiological signal measurement. Strong adhesion is achieved without any chemical treatment by gently applying a low preload pressure to the electrode, ensuring sufficient bonding. The high conductivity of the skin-conformal conductor, combined with the close adhesion provided by the OIA, guarantees low skin impedance, facilitating the accurate capture of individual physiological signals. (iii) A lightweight 2.8 g FPCB made from a polyimide substrate was designed for signal collection and wireless data transmission, making it suitable for skin attachment. It processed signals independently using a battery and transmitted filtered data via Bluetooth Low Energy (BLE) to a smartphone for machine-learning-based disease diagnosis.

Fig. 1b shows a scanning electron microscope (SEM) image of the stretchable conductors with different combination. A blend of organic and inorganic materials was formulated in optimized proportions and fabricated following the sequential steps detailed in Fig. S1. To achieve excellent conductivity and elongation, the material composition was optimized by observation of different composition of conductors: conductor containing silver paste (SP, composed of 70 wt% Ag flakes in WPU with a surfactant at 1/30 of the Ag content.), conductor containing silver paste and conductive polymer (SP/CP, 5 wt% CP composed of PEDOT:PSS with a ethylene glycol ((CH₂OH)₂) at 1/20 of the PEDOT:PSS content in SP), conductor containing silver paste and ionic liquid (SP/IL, 18 wt% ionic liquid in SP), and conductor containing silver paste, conductive polymer, and ionic liquid (SP/CP/IL). The addition of conducting polymer in matrix (SP/CP) shows a similar distribution of Ag flakes in WPU, while IL caused Ag flake aggregation with irregular distribution. To evaluate electrical performance (Note S1) and stretchability (Note S2), various conductor compositions were tested, as shown in Fig. 1c, d. Compared to SP, SP/CP significantly improved electrical properties because the highly conductive linear PEDOT chains formed by phase separation between PEDOT and PSS help electrical connection between Ag flakes [23]. However, the reduced stretchability of SP/CP is due to the poor elongation capacity of PEDOT:PSS, typically less than

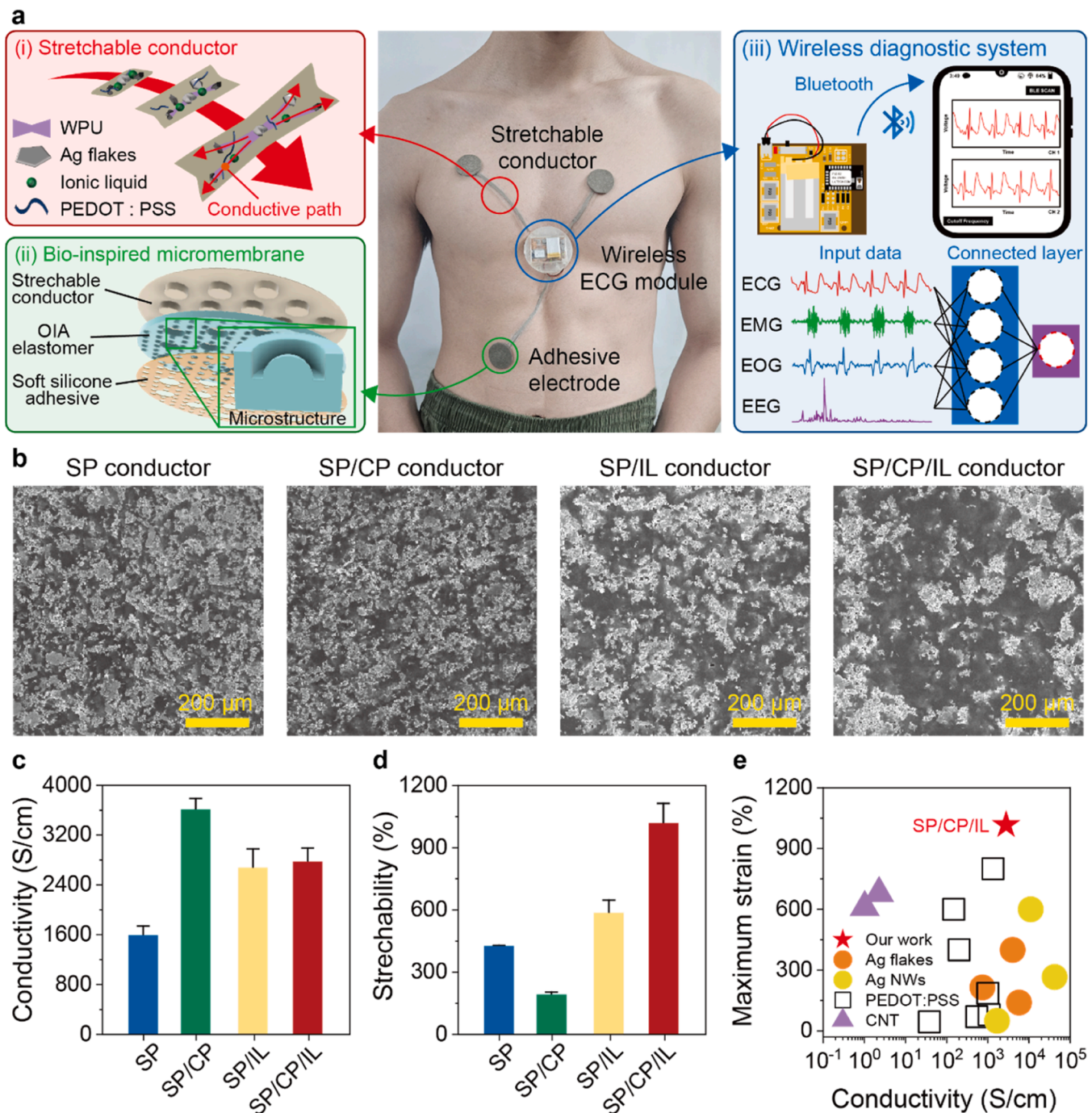


Fig. 1. Wireless vital-monitoring system with machine learning and conductive material design. a, Schematic of wireless vital monitoring system with machine learning using stretchable conductor and bioinspired micromembrane architecture. b, SEM images of SP, SP/CP, SP/IL, and SP/CP/IL conductor. c-d, (c) Conductivity and (d) strain of SP, SP/CP, SP/IL and SP/CP/IL conductor. e, Conductivity and strain comparison between the stretchable conductor using materials with long-term stability reported in the literature and the one in this work (SP/CP/IL conductor).

2 % [24]. The inclusion of IL in SP (SP/IL) reinforced the WPU-based matrix, enhancing strain tolerance by forming a flexible yet robust conductive network [25]. However, the addition of IL increased impedance at the skin-electrode interface (Fig. S2 and Note S3). To achieve an optimal balance between electrical performance, mechanical durability, and bioimpedance, the composition of SP, CP, and IL was systematically optimized. Ag flakes formed a percolative conductive network, while PEDOT:PSS and ethylene glycol enhanced interparticle connectivity, minimizing contact resistance. WPU provided high stretchability (up to 800 %) and elasticity, ensuring the conductor's mechanical stability under strain. The addition of IL further optimized

the flexible network by reducing stress concentration, preventing crack formation, and improving elasticity. As a result, the SP/CP/IL conductor exhibited an initial conductivity of 2768 S/cm and an exceptional stretchability of 1016 %, surpassing other state-of-the-art stretchable conductors (Fig. 1e, Table S1). The SP/CP/IL conductor demonstrated uniform dispersion of conducting polymer with IL facilitating electrical connections between aggregated Ag flakes, as confirmed by TEM and EDS mapping (Fig. S3). These enhancements in mechanical stretchability and durability [26] make it ideal as a stretchable interconnector for personalized vital monitoring systems, offering exceptional stretchability and adaptable attachment.

3. Electrical and mechanical characterisation of stretchable conductors

Fig. 2a-c respectively show the conductivity, strain, and Young's modulus of the conductor, with a 350 μm thickness was used. As thinner

conductors exhibit lower elongation, we chose a thickness that balanced the minimal thickness with a high strain (Fig. S4). We optimized the elemental composition of the SP/CP/IL conductor to achieve both high electrical conductivity and mechanical durability. Increasing the Ag flake concentration enhanced conductivity up to 70 wt%. However,

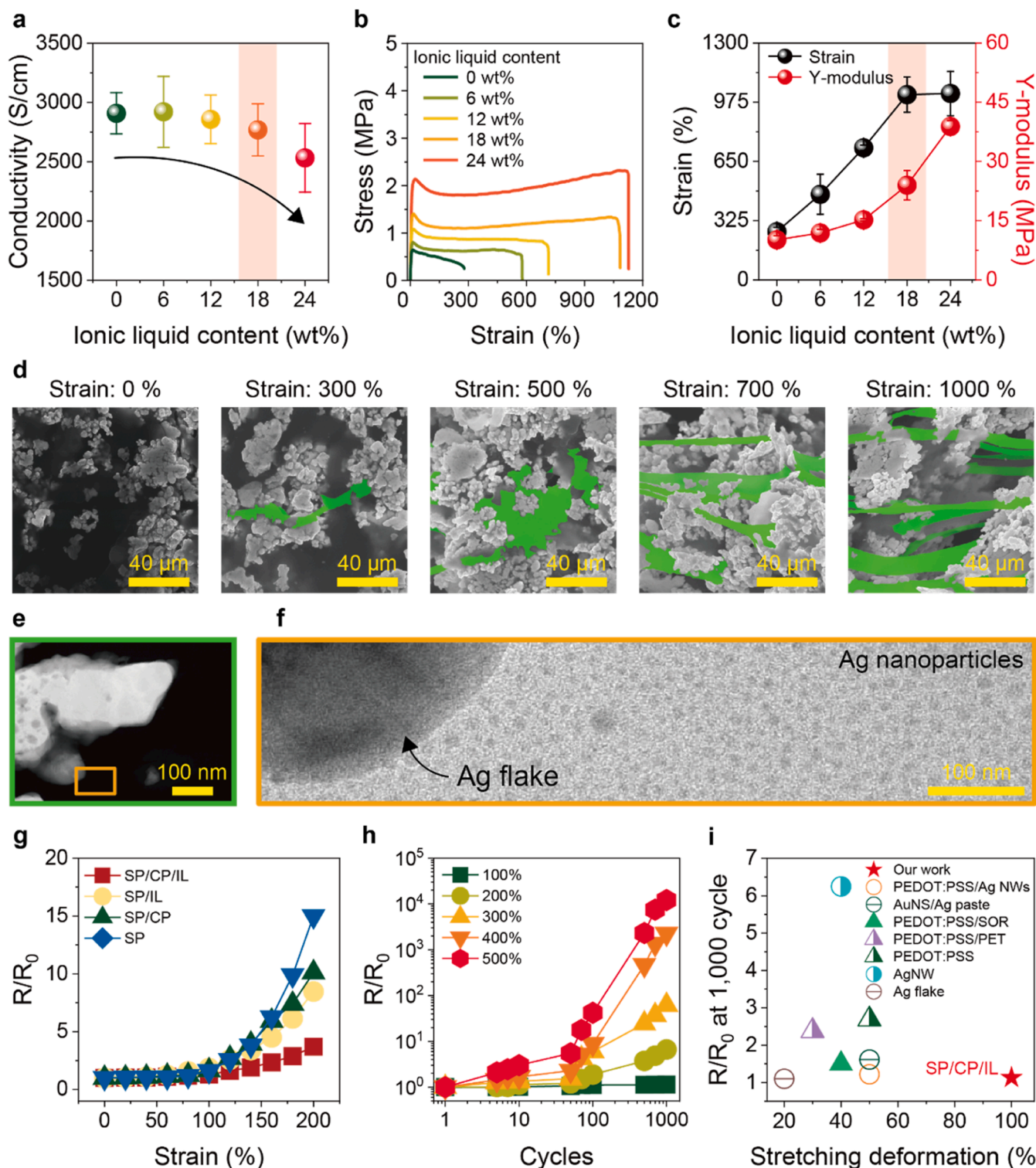


Fig. 2. Electrical and mechanical analyses of stretchable conductors. (a) Conductivity, (b) strain-stress curve, (c) strain and Young's modulus of the stretchable conductor with the ionic liquid-content variation. d, SEM images of stretchable conductors in the tensile strain from 0 % to 1000 %. Conductive paths (green color) are composed of WPU and conductive materials. e-f, TEM images of stretchable conductor. Conductive paths are composed of (e) Ag flake and (f) Ag nanoparticles. g-h, Rate of resistance changes for SP/CP/IL, SP/CP, SP/IL and SP conductors (g) under different tensile strain and (h) after repetitive cycles of stretching-release. i, Rate of resistance change at 1,000 cycles comparison between the stretchable conductors reported in the literature and the one in this work (SP/CP/IL conductor).

miscibility issues emerged beyond this threshold, leading to the identification of an optimal ratio of 7:3 for Ag flakes to WPU (Fig. S5a and Table S2). For the SP/CP conductor, incorporating 5 wt% CP achieved an optimal balance between conductivity and stretchability (Fig. S5b and Table S3). Similarly, for the SP/IL conductor, 18 wt% IL was determined to provide maximum stretchability without encountering dispersion issues (Fig. S5c and Table S4). After determining the ratios of SP/CP and SP/IL, compositional studies on IL ratios of 0–24 wt% in SP/CP polymer were conducted to determine the optimal concentration in the SP/CP/IL conductor. The conductivity gradually decreased with increasing IL content, with a significant drop observed at 24 wt% IL (Fig. 2a). Additionally, the stretchability increased with higher IL content, reaching saturation at 18 wt% IL (Fig. 2b). As the IL content increased, Young's modulus, which reflects the stiffness of the conductor within the elastic region where the material recovers its original shape after deformation, gradually increased (Fig. 2c). This improvement is attributed to the strong intermolecular interactions between IL and WPU, which enhance internal cohesion [27]. IL also promotes uniform stress distribution, reducing localized strain concentration and contributing to improved mechanical elasticity. The conductor with 18 wt% IL was optimized to achieve the best balance between electrical performance and mechanical robustness, ensuring stable operation under deformation (Table S5). At the optimized composition, the conductor maintained stable electrical properties for 30 days in air without being stored in special environments. During this period, humidity fluctuated between RH 35 % and RH 75 %, but no significant change in electrical resistance was observed, confirming the conductor's robustness under typical environmental conditions (Fig. S6). Additionally, Poisson's ratio of 0.046 was observed during stretching (Fig. S7).

For use as a stretchable interconnector in physiological signal monitoring, it is essential that the optimized SP/CP/IL conductor retains robust electrical properties under deformation. SEM images taken across a strain range of 0–1000 % (Fig. 2d), demonstrate that the conductive pathways (highlighted in green) stretch uniformly with applied strain, maintaining structural integrity without damage. Additionally, energy-dispersive X-ray spectroscopy (EDS) analysis in Fig. S3 confirms the homogeneous distribution of WPU, PEDOT:PSS, and ionic liquid throughout the matrix. Since the conductive pathways arise from the embedded conductive materials within the WPU framework, the green-highlighted regions can be identified as the primary conduction networks. Interestingly, this robust conductive path is reinforced by well-dispersed Ag nanoparticles (Fig. 2e, f) embedded throughout the matrix at the nanoscale, significantly enhancing both mechanical and electrical stability. As shown in Fig. 2g, the electrical properties of the SP/CP/IL conductor demonstrate superior performance under stretching conditions ranging from 0 % to 200 %, measured in 20 % increments. The SP/CP/IL conductor exhibited a mere 1.29 % change in resistance at 100 % deformation and 3.7 % at 200 %, indicating superior electrical performance compared to other types of conductors.

For practical applications, it is crucial to maintain stable electrical properties under repeated deformation. Considering the mechanical behavior of the conductor under various strain rates, a deformation speed of 1 mm/s was applied (Fig. S8a). Although the elastic deformation range is below 100 %, the damage-tolerant design with nanoscale stretchable conductive pathways allows the conductor to maintain meaningful mechanical response under repeated large deformations (Fig. S8b). As a result, the conductor remains structurally and electrically stable throughout the cycles (Fig. S9). As shown in Fig. 2h, specifically, at 100 % strain, resistance changed by only 1.13 % after 1000 cycles, indicating excellent durability. The resistance change rate increased significantly after 1000 cycles of repetitive mechanical strain at 400–500 % due to higher stress levels causing fatigue and micro-structural damage [28]. In contrast, the minimal resistance changes at 100–300 % strain indicate these lower levels remained within the material's elastic limit, maintaining stable electrical properties without significant damage [29]. Compared to previously reported stretchable

conductors, our conductors exhibited superior electrical performance under large strains and high operational stability below 100 % repetitive deformation (Fig. 2i and Table S3). Overall, the robust conductive path (Fig. 2d) and uniform Ag NPs distribution (Fig. 2f) ensure stability up to 200 % strain, allowing reliable electrode placement while minimizing cracks and abrupt resistance increases. This guarantees reliable electrode placement, tailored to individual physical dimensions, while minimizing the impact of cracks and preventing abrupt resistance increases.

4. Bioinspired monolithically interlocked skin-compatible adhesive

To achieve long-term, repeatable, and user-friendly physiological signal monitoring, we developed a soft, non-toxic OIA elastomer interlocked with stretchable conductors (Fig. 3a, b). The OIA structure (fabrication details in Fig. S10, S11) provides stable skin adhesion and multifunctional skin-conformal features, including air permeability, deformability, and moisture tolerance (Video S1). Physical adhesion is achieved through internal negative pressure generated by structural deformation during preloading (Fig. 3c). FEM simulations show that strong intermolecular interactions between the 40- μ m-radius dome and the 50- μ m-radius inner chamber result in substantial internal pressure changes. This effect is induced even with a minimum preload of 5 kPa (Fig. 3d and Note S4), leading to stable internal negative pressure within a single OIA (see Note S5 for details) [30–32].

Supplementary material related to this article can be found online at [doi:10.1016/j.mser.2025.101059](https://doi.org/10.1016/j.mser.2025.101059).

To confirm the enhanced skin adhesion of the OIA elastomer, adhesion strength was tested for elastomers (diameter of 3 cm) with different interfacial structures (Note S6) on a Si wafer and a rough pig-skin replica (Fig. S12 and Note S7, S8). The evaluation included six different structural configurations: flat, chamber-only, and chamber with a dome structure (OIA), each tested with and without surface treatments (MED-6342), at a preload of 5 kPa, where adhesion typically reached saturation. (Fig. S13). The results in Fig. 3e show that the OIA elastomer achieved markedly higher adhesion (~8.84 kPa) compared to chamber-only (~6.56 kPa), flat structure (~2.7 kPa), and the as-fabricated stretchable conductor (S.C., ~1.9 kPa) on pig skin replica. Beyond its structural advantages, the OIA elastomer coated with MED-6342 (M-OIA) demonstrated enhanced adhesion, with an approximate increase of 26 % in dry conditions (relative humidity ~50 %) and 32 % in wet (artificial glandular sweating) conditions (Fig. S14 and Note S7) with lower skin impedance (Fig. S15, Fig. S16 a-c).

The areal occupancy of the stretchable conductor in the interlocked structure, the ratio between hole size and spacing-must be optimized for strong skin adhesion and low interfacial electrical impedance. When only the conductor diameter was varied in a hexagonal array while maintaining a 20 % conductor-to-adhesive occupancy ratio, optimizing the conductor diameter to 3 mm achieved the highest adhesive performance, exceeding 9 kPa under dry conditions and 5.4 kPa under wet conditions (Fig. 3f and Fig. S17). While slightly lower than the adhesion of the OIA structure alone (Fig. 3e), the 3-mm diameter ensured stable interlocking and even stress distribution, reducing stress concentration and separation during detachment, as shown in FEM simulations. (Fig. 3g, Fig. S18 and Note S10).

In addition to diameter control, tuning the SR (conductor-to-adhesive occupancy ratio) is also crucial (Fig. 3h and Fig. S19). When the SR dropped below 1, both pulling and shear adhesion performance significantly decreased on various surfaces under dry and wet conditions (Fig. 3i, j, Fig. S20 and Note S8), due to a smaller area of OIAs (Fig. S21 and Note S11, S12). In contrast, an SR of 2 (occupancy ratio of ~7 %) demonstrated reliable adhesion but resulted in lower bioimpedance at the skin interface (Fig. S22). As a result, SR of 1 exhibited minimal changes in adhesive force after 1000 attachment-detachment cycles (Fig. S23 and Video S2) with low skin impedance values of $8.9 \times 10^5 \Omega$

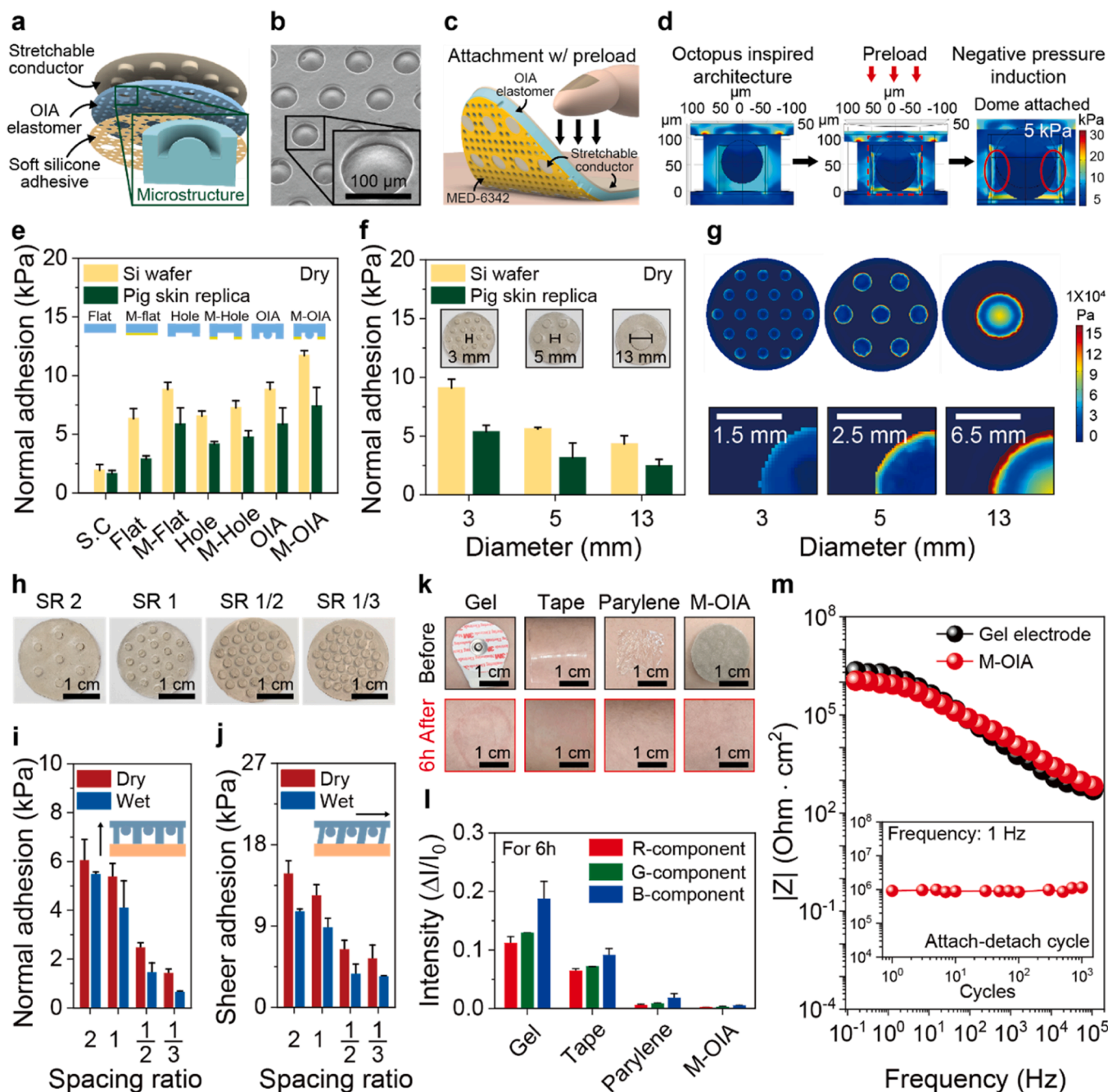


Fig. 3. Structural optimization procedure of octopus suckers inspired micromembrane architecture (OIA) and evaluation of skin irritation. **a**, Schematic of the bioinspired micromembrane structure. **b**, SEM images of OIA. Inset shows a close-up view of single OIA. **c**, Illustration of the micromembrane structure attachment with preloading. **d**, FEM simulation for the structural behavior of OIA through preloading. **e**, Normal adhesion of various adhesive architectures against a Si wafer (yellow) and pig skin replica (green) under dry condition; $N = 10$. **f**, Normal adhesion according to the different conductor diameters of M-OIA against a Si wafer (yellow) and a pig skin replica (green) under dry condition; $N = 10$. **g**, FEM simulation of the stress concentration on conductors (spacing ratio: 1) with different diameters (3 mm, 5 mm, 13 mm) under detachment processes. **h**, Photographs of M-OIA electrode with different spacing ratios (SR: 2, 1, 2/1, 1/3). **i**, Normal adhesion of M-OIA electrode with different spacing ratios against a pig skin replica under wet condition; $N = 10$. **j**, Shear adhesion of M-OIA electrode with different spacing ratios against a pig skin replica under wet condition; $N = 10$. **k**, Photograph of comparative observations for skin irritation (redness) after 6 h attachment of various adhesives (gel electrode, plastic tape, parylene and M-OIA electrode). **l**, The ratios of colorimetric intensities (red, green, blue) of skin images. **m**, Impedances according to the frequency changes (1 Hz ~ 100 kHz) of gel electrode and M-OIA electrode. Inset shows the impedances of 1 Hz over 1000 cycles of attachment/detachment.

cm^2 at 1 Hz. It also supports a weight of 100 g (Fig. S24) and withstands 0–200 % elasticity when attached to the skin, making it suitable for wireless diagnostic systems (Fig. S25).

Supplementary material related to this article can be found online at [doi:10.1016/j.mser.2025.101059](https://doi.org/10.1016/j.mser.2025.101059).

To verify skin-interface compatibility under practical application

conditions, we evaluated skin irritation levels after long-term attachment (24 h) of the electrode to real human skin. The analysis of normalized intensity change ($\Delta I/I_0$) in skin color showed minimal irritation, demonstrating better skin compatibility than commercial adhesives and other skin-compatible substrates (Fig. 3k, l, Fig. S26, 27 and Note S13). No material residue was observed after 12 h of skin

attachment (Fig. S28), confirming the safety of the electrode for extended use. To further evaluate cytocompatibility, a surface-mediated viability test was performed. The M-OIA electrode was first placed on a sterile coverslip and incubated for 12 h. After removal of the electrode, NIH3T3 fibroblast cells were seeded onto the same coverslip and cultured for 24 h. Cell viability, assessed using a Live/Dead assay, was approximately 97.6 % relative to the control group, indicating good cytocompatibility of the material (Fig. S29, Note S14 and S15). Furthermore, Fig. 3m and Fig. S16d–f demonstrate that the M-OIA electrode exhibits lower impedance than the gel electrode, and approximately 20 % lower PSD of the impedance signal, supporting its suitability for biopotential signal acquisition. Since bioelectrodes are typically applied under controlled conditions to ensure stable skin

contact for physiological signal acquisition, testing under extreme environmental conditions may not accurately reflect real-world usage. Instead, we focused on verifying adhesion stability under repeated detachment scenarios. Throughout 1000 attachment-detachment cycles, the M-OIA electrode exhibited minimal skin irritation and maintained low skin impedance, comparable to commercial gel electrodes (Fig. 3m) on human skin, confirming its suitability for long-term physiological monitoring.

5. Wireless ultra-light FPCB for ECG, EMG, EOG, and EEG signal monitoring

Fig. 4a shows an FPCB for wireless bio-signal monitoring by

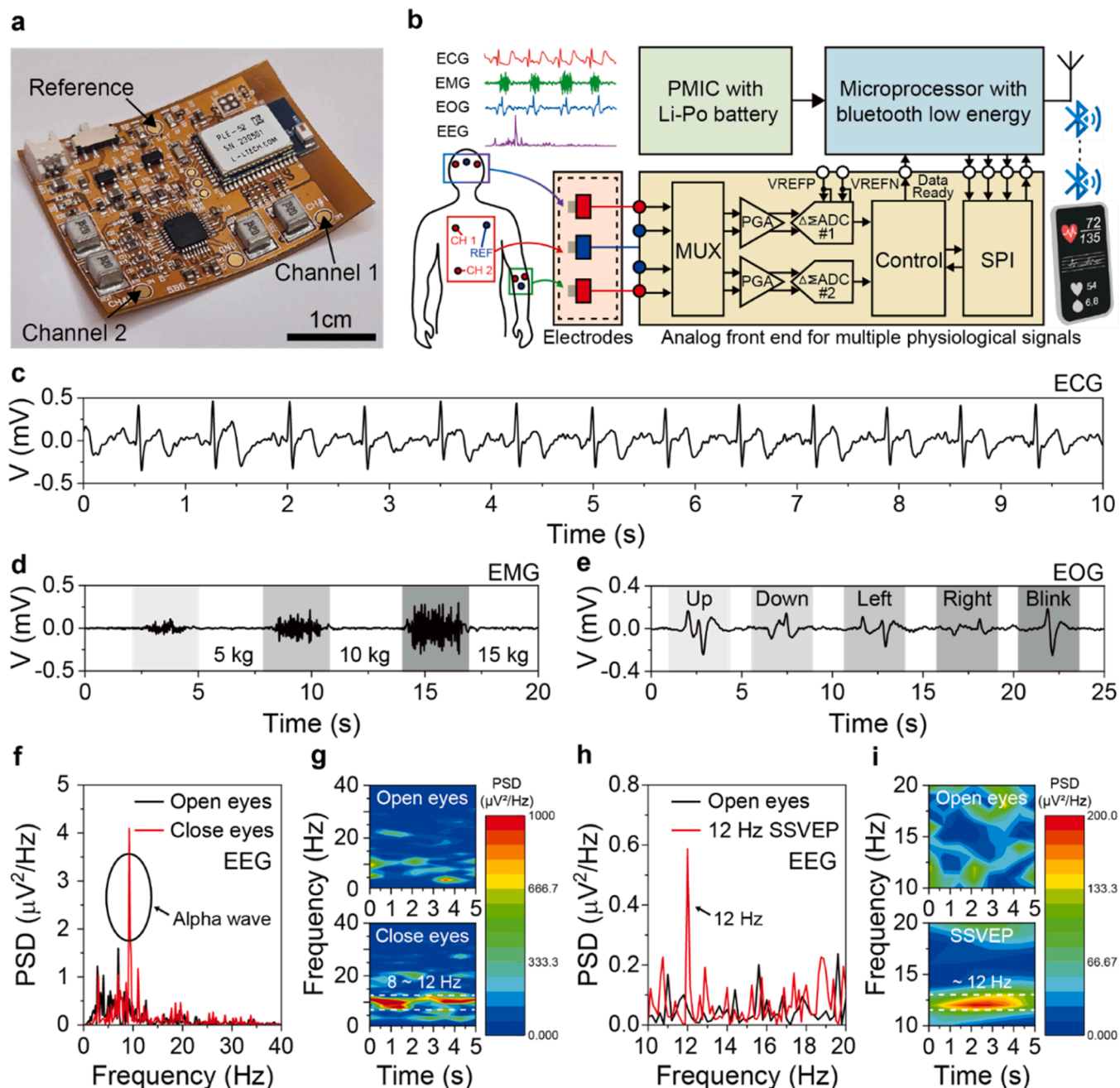


Fig. 4. Wireless biomonitoring of ECG, EMG, EOG and EEG. **a**, Photograph of wireless bio-monitoring system. **b**, Schematic of system-level block composed of electrodes, a readout module, BLE microcontrollers, and a PMIC. **c**, ECG signals using wireless bio-monitoring system. **d**, EMG signals in the muscle strength from 5 kg to 15 kg. **e**, EOG signals of eye movements (up, down, left, right and blink). **f–g**, EEG signals in the eye open/close paradigm of (f) power spectrum density and (g) spectrogram. **h–i**, EEG signals in SSVEP paradigm (12 Hz) of (h) power spectrum density and (i) spectrogram.

integrating a stretchable interconnector and skin-interfaced M-OIA electrode at channel and reference points (Fig. S30). The FPCB module, sized at 4 cm × 2.5 cm and weighing 2.8 g, is encapsulated with a top polymeric cover and a base M-OIA elastomers for tight skin adhesion (Fig. S31). Fig. 4b presents a block diagram of the wearable device for multisite physiological signal monitoring, including ECG, EMG, EOG, and EEG. The wearable device consists of four functional parts: electrodes, a readout module, a microprocessor with Bluetooth low energy (BLE), and an external power management integrated circuit (PMIC) with a Li-Po battery. The electrodes capture bio-signals from multiple body locations, and to ensure high-quality data, the amplifier's voltage gain is programmable to accommodate signals ranging from microvolts to millivolts. A multiplexer (MUX) and programmable gain amplifiers (PGAs) adjust both gain and input range based on the specific physiological signal type. These analog signals are then digitized through sigma-delta ($\Delta\Sigma$) analog-to-digital converters (ADCs). The microcontroller (MCU) reads the resulting digital data via a serial-to-parallel (SPI) interface, which is subsequently transmitted to a portable device through BLE communication. With the optimized power management IC (PMIC), the wearable device consumes an average of 76 mW in continuous monitoring mode, enabling stable operation for over 8 h on a single charge. In intermittent monitoring mode, where measurements occur at designated intervals rather than continuously, power consumption is reduced, allowing for extended battery life beyond 8 h, depending on the duty cycle and sleep-state efficiency. The system operates using a replaceable Li-Po battery (MP422025P; 3.7 V; 180 mAh), ensuring flexible usage in both monitoring modes.

Maintaining stable measurements of various physiological signals without crosstalk between channels is crucial. Therefore, the electrodes were carefully positioned based on the physiological origins of each signal. Additionally, impedance balancing between electrodes was employed to effectively cancel common-mode noise, and digital signal processing techniques were used to improve crosstalk reduction. The fully integrated system applied to the chest (Fig. 1a) enabled real-time wireless ECG monitoring (Fig. 4c). PSD analysis of the ECG signals revealed a clear peak at the QRS complex, a defining feature of cardiac activity (Fig. S32a). The system demonstrated mechanical durability, providing stable signal acquisition even when directly attached over the heart. Reliable ECG measurements were sustained as the stretchable conductor was twisted, bent, and stretched up to 300 % and the measured ECG signals were transmitted to a portable electronic device (Video S3). Furthermore, stable ECG signals were consistently acquired during various movements such as walking, running, and repeatedly sitting and standing while the system was worn (Fig. S33). For the second application, we demonstrated EMG-signal monitoring using an M-OIA electrode as an EMG sensor (Fig. S34). The highly adhesive M-OIA electrode improves skin contact, reducing motion artifacts and enhancing EMG signal acquisition. Fig. 4d shows the lightweight, flexible system for sensitive EMG monitoring, with forces of 5, 10, and 15 kg applied. The peak-to-peak amplitude and intensity of the EMG signal increased with the applied force (Fig. S35a). Analysis of the root mean square (RMS) values revealed that RMS increased with greater applied force, while the system effectively detected lower-amplitude EMG signals from smaller forces (Fig. S35b). A distinct peak appeared in the low-frequency range of the EMG signal PSD, while minimal spectral power was observed above 250 Hz, indicating that muscle contractions were measured with high clarity and low noise (Fig. S32b). For our third application, we monitored EOG patterns and their distinct movements (Fig. 4e), with the FPCB and electrode positioned on the forehead (Fig. S36). The analysis revealed recognizable EOG patterns for different eye movements, including up, down, left, right, and blinking, with amplitude variations due to position and force differences (Fig. S37). For the EOG signals, PSD analysis revealed notable low-frequency peaks during eye movements, contrasting clearly with resting states and validating the accurate detection of ocular activity (Fig. S32c). The EOG signals, showing voltage changes in the millivolt range, highlight the

potential for applications in medical diagnostics, sleep studies, and cognitive research. For our final application, we focused on EEG signal monitoring, a noninvasive method to measure brain electrical activity. The EEG signals were acquired using the same conditions as the previous EOG experiment (Fig. S36). In a stable condition, representative EEG patterns across frequency bands were confirmed (Fig. S38). Fig. 4f shows a strong alpha wave around 10 Hz, indicating a relaxed state, verified by PSD analysis. EEG spectrograms (Fig. 4g and Video S4a) provide detailed PSD information over time within the 8–12 Hz range. Additionally, steady-state visual evoked potentials (SSVEPs) were captured by monitoring EEG responses to a 12 Hz flashing stimulus, demonstrating exceptional sensitivity (Fig. 4h, i and Video S4b). Overall, the lightweight design, durable FPCB, low electrode-skin impedance, and stable, stretchable conductor enable accurate real-time bio-signal monitoring. Additionally, the electrode maintains consistent conductivity, adhesion, and low impedance even after 7 days, allowing reliable bio-signal acquisition with a high SNR of approximately 39 dB (Fig. S39), making it suitable for long-term wearable health applications.

Supplementary material related to this article can be found online at [doi:10.1016/j.mser.2025.101059](https://doi.org/10.1016/j.mser.2025.101059).

6. ECG-based cardiac health classifier for health assistance

Beyond wireless vital monitoring, we directly analyzed ECG signals to validate a disease classification algorithm designed for early detection of cardiac conditions and timely intervention. Fig. 5a shows an intelligent cardiac health classifier that distinguishes between normal and abnormal conditions in a dataset labeled with four cardiac classes: normal (N), atrial fibrillation (AF), sinus tachycardia (ST), and ventricular fibrillation (VF). To achieve high classification level, we integrated one-dimensional (1-D) time-series data analysis with two-dimensional (2-D) image classifier. First, ECG signals underwent pre-processing steps, including filtering, normalization, and baseline-wander removal, to ensure data quality (Note S16). In the 1-D time-domain analysis, the pre-processed ECG signals were divided into 30-second (30-s) intervals with a sliding window technique [33]. Then, R-R intervals (RRI) were determined using a peak detection algorithm to measure the time between heartbeats. A Poincaré plot is an effective tool for visualizing heart rate variability geometrically. Two adjacent RR intervals (RRI_n , RRI_{n+1}) are plotted in a scatter plot. From 30-second intervals, the standard deviation of normal-to-normal (SDNN) index values was derived from the Poincaré plot, with the SDNN threshold used to screen for AF and VF based on heart rate variability. For 2-D image classification, 4-second ECG segments were converted into spectrograms using short-time Fourier transform (STFT) to capture frequency characteristics. The 4-second duration was selected for analysis based on achieving the highest accuracy in the confusion matrices (Fig. S40). These spectrograms were subsequently classified through a transfer learning approach using a VGG-16 model. The transfer learning process is outlined in Fig. 5b and Fig. S41. VGG-16 was originally trained on the ImageNet database, enabling it to recognize 1000 different patterns from millions of labeled images [34]. In our approach, we employed transfer learning by retraining the final fully connected (FC) layer of VGG-16 to efficiently classify ECG data. This model leveraged transfer learning with large-scale data instances to enhance classifier performance. By effectively handling noise without distorting signal waveforms, it achieved high accuracy in predicting four cardiac classes: N, AF, ST, and VF. The representative Poincaré plots (Fig. 5c) reveal that AF and VF intervals display irregular patterns with greater dispersion compared to N and ST, as further illustrated in Fig. S42. The average SDNN index values for the N, AF, ST, and VF classes were identified as 50.77 ms, 139.34 ms, 65.38 ms, and 225.88 ms, respectively (Fig. 5d). Notably, the SDNN values for AF and VF were significantly higher than those for N and ST, highlighting substantial differences in cardiac variability (Fig. S43). VF signals exhibit distorted peak shapes, including

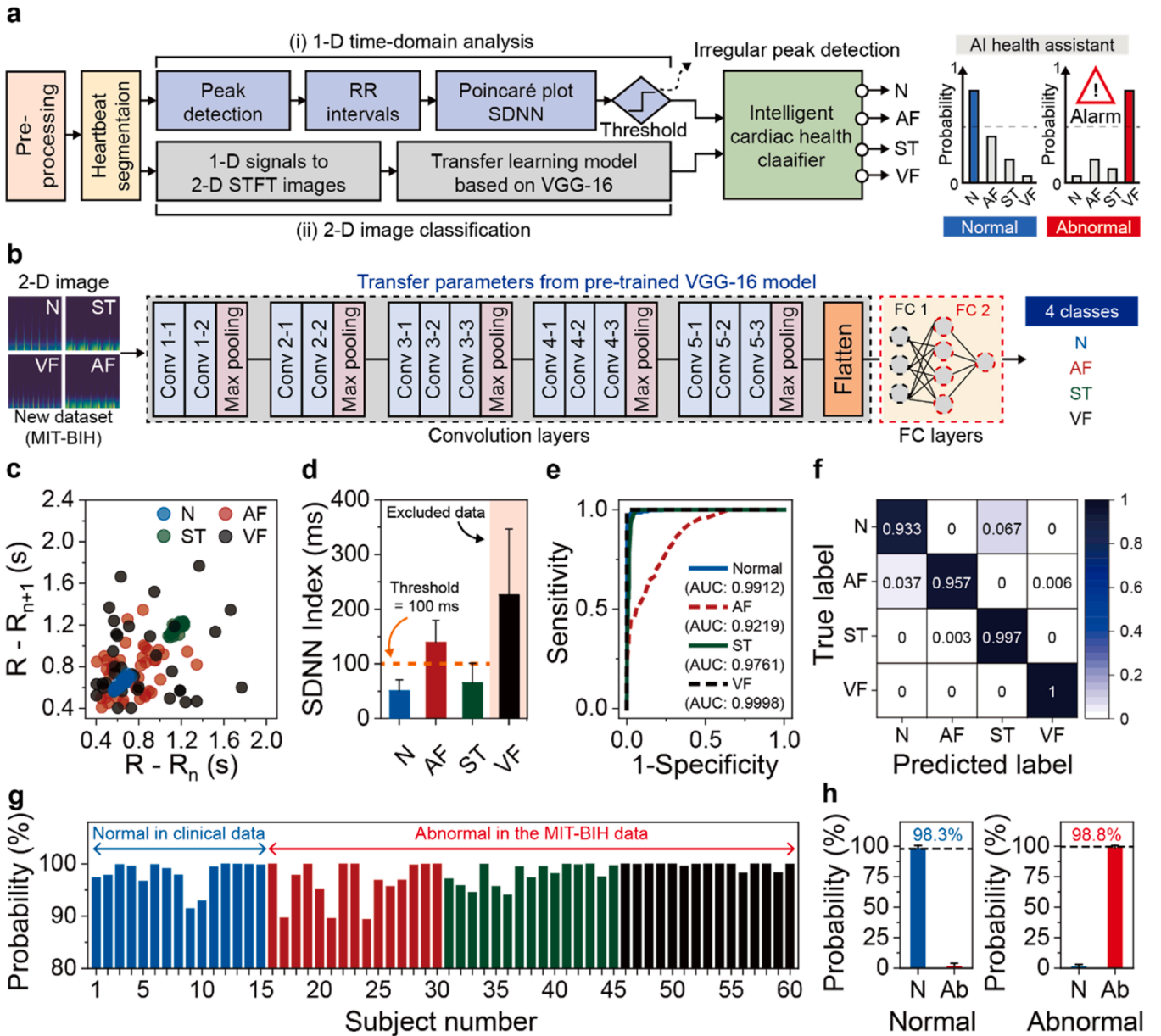


Fig. 5. ECG-based Cardiac Health Classifier for artificial intelligence health assistance. **a-b**, Schematic of (a) intelligent cardiac health classifier with 1-D time domain analysis and 2-D image classification and (b) transfer learning-based 2-D image classification process. **c-d**, The 30-s (c) Poincaré plots and (d) bar plots of the standard deviations of R-peak intervals for normal, AF, ST, and VF, respectively. **e**, ROC curves of the normal and abnormal datasets. **f**, Confusion matrix for normal (N) from clinical datasets and abnormal rhythms (AF, ST, VF) from the MIT-BIH datasets. **g**, Probability for the fifty subjects with the top 15 ranked probabilities from normal and abnormal subjects. **h**, Bar plots for the averaging probability of normal and abnormal groups, respectively.

unclear QRS complexes and R-peaks, aiding in differentiation from AF by highlighting irregular VF patterns. A 100 ms SDNN threshold was set for AF detection, improving the model's ability to distinguish between these arrhythmias based on their unique variability signatures. The ROC curve, resulting from 2-D classification, illustrates the performance of the binary classifier by plotting the true positive rate (sensitivity) against the false positive rate (1-specificity) across various thresholds, thereby assessing the classifier's ability to distinguish between classes. Fig. 5e shows ROC curves for four classes (N, AF, ST, VF) using a 4-second time frame. The classifier achieved an area under the curve (AUC) above 0.989 for N, ST, and VF, demonstrating high classification accuracy. Although the AUC for AF was 0.8667, lower than the other classes due to its similarity to normal signals, the integration of 1-D time-series analysis with 2-D image classification improved AF detection by leveraging heart rate variability (HRV) metrics. Specifically, SDNN thresholding

from the Poincaré plot was used as an additional screening method to enhance AF classification. Through this decision-level fusion approach, the overall classification accuracy improved by 17.55 % compared to previous methods, demonstrating superior sensitivity and specificity across various cardiac conditions in both the MIT-BIH and clinical datasets (Note S17, and Fig. S44, S45, S46). As illustrated in Fig. 5f, the confusion matrix shows a classification accuracy of 93.3 % for normal (N) data and 98.5 % for abnormal data (AF, ST, and VF) collected from 67 participants. Normal data were collected in a clinical setting using a wireless cardiac monitoring system developed in this study (Note S18), while abnormal data were obtained from publicly available MIT-BIH datasets. Fig. 5g presents the probability plots of the predicted labels for each class based on 15 subjects, along with the average probabilities for normal and abnormal groups. We analyzed the probability of each individual ECG data point (15 for each condition) being classified as N,

AF, ST, or VF (Fig. S47–S51). The results highlight our system's capability to accurately classify normal and abnormal conditions, achieving probabilities of 98.3 % and 98.8 %, respectively (Fig. 5h).

7. Conclusions

This study addresses key challenges in long-term wearable bio-sensing systems by integrating a robust network of stretchable conductors, bioinspired skin-adhesive electrodes, an ultralight wireless flexible printed circuit board (FPCB), and a machine learning-based dual-method disease classification approach. The system offers remarkable adaptability in electrode positioning, accommodating variations in body size through highly stretchable conductors. The use of an organic-inorganic hybrid matrix ensures both mechanical durability and minimal resistance change during stretching. The bioinspired architecture, when interlocked with the stretchable conductor, enhances skin-conformability and adhesion, maintaining performance even after 24 h of continuous attachment. A lightweight, wireless FPCB enables seamless capture of diverse physiological signals—ECG, EMG, EOG, and EEG—while machine learning algorithms accurately classify ECG signals with 93.3 % accuracy through the SDNN index and STFT image analysis. As the demand for advanced wearable health monitoring and diagnostic systems rises, innovations such as this pave the way for more efficient, durable, and personalized solutions in real-time health diagnostics and disease management.

8. Materials and Methods

8.1. Materials and reagents

Ag flakes (> 99.99 %, DSF-500 MWZ) were purchased from DAEJOO ELECTRONIC MATERIALS Co. Ltd. PEDOT: PSS (Clevios PH 1000) was purchased from Heraeus Co, Ltd. The surfactant (SURFLON S-386) was obtained from AGC Seimi Chemical Co., Ltd. WPU (WPU-2101) was supplied by ALBERDINGK BOLEY Co., Ltd. $(\text{CH}_2\text{OH})_2$ and EMIM-TFSI (> 98 % (HPLC), 1-Ethyl-3-methylimidazolium bis(trifluoromethylsulfonyl)imide) were obtained from Sigma-Aldrich. NIH-3T3 (Korean Cell Line Bank), Microscope cover glasses, cover slip (12 mm Φ , Marienfeld GmbH & Co.); Dulbecco's modified eagle medium, DMEM (1X, high glucose, pyruvate, Gibco™); Penicillin–streptomycin solution, Pen/Strep (10,000 units/mL Penicillin, 10,000 $\mu\text{g/mL}$ Streptomycin, Hyclone); Fetal bovine serum, FBS (South America origin, Thermo Fisher Scientific) Calcein-AM (Thermo Fisher Scientific); Ethidium Homodimer-1 (Thermo Fisher Scientific).

8.2. Fabrication of stretchable conductors

To fabricate a stretchable conductor, PEDOT:PSS was mixed with $(\text{CH}_2\text{OH})_2$ and stirred vigorously for 5 min. EMIM TFSI was then added, and the mixture was further stirred at room temperature for 2 h. Subsequently, Ag flakes, WPU, and a surfactant were added and the mixture was stirred at room temperature for 48 h. A Si mould was used as the substrate to facilitate simple peeling. The blend filler that was thus prepared was drop-cast into a Si mould to fabricate an SP/CP/IL conductor, which was then dried at 60 °C for more than 4 h. Finally, the SP/CP/IL conductor was peeled off the mould. For the SP, SP/CP, and SP/IL conductors, the constituent materials were varied and fabricated as described above.

8.3. Fabrication of the M-OIA electrode

To fabricate the M-OIA electrode, the previously fabricated and patterned adhesive part was placed on the release film with the OIAs facing downward. Subsequently, the stretchable conductor material was poured onto the prefabricated adhesive until the back was completely filled. A vacuum of up to -1 MPa was formed to allow the conductor

material to permeate uniformly. The M-OIA electrode was finally obtained after baking for 6 h at 60 °C.

8.4. ECG, EMG, EOG, and EEG signal measurement

To monitor ECG, M-OIA electrodes were connected to the FPCB module via a stretchable conductor and attached near the heart. Signals were processed with low-pass (20 Hz), high-pass (0.5 Hz), and band-stop (59–61 Hz) filters, and stabilized using a 1 Hz high-pass filter. For EMG, electrodes on the left hand underwent similar filtering (low-pass 100 Hz, high-pass 0.5 Hz, band-stop 59–61 Hz), with a final 1 Hz filter for baseline stabilization. For EOG and EEG monitoring, electrodes were attached to the forehead, following the same filtering process used for EMG. Additionally, for EEG, a band-pass filter (3–40 Hz) was applied to observe alpha waves.

8.5. Machine-learning development

The machine-learning system employed a dual approach, using a transfer-learning-based classifier and an SDNN index-based thresholding method to distinguish normal and abnormal ECG signals. Acquiring large labelled ECG datasets is costly, so transfer learning with a VGG-16 network pretrained on ImageNet was used. The system consists of: (1) Thresholding method: SDNN index values were extracted from 1-D ECG signals using R-peak detection via NeuroKit2, and Poincaré plots were utilized for AF detection. Finally, the SDNN index values are calculated from the R-peak intervals and locations. (2) Transfer learning-based classifier: ECG signals were transformed into 2-D STFT spectrograms. A VGG-16 network, with pretrained weights up to the first fully connected layer, was retrained on 7300 image-data points from 40 ECG sections (N, AF, ST, VF). The final layer was trained using a softmax activation function, with a batch size of 30 and a learning rate of 0.01 for five-fold cross-validation.

Code Availability

We provide the code utilized in this study to support public availability, which can be deposited in a public repository of *Materials Science and Engineering: R: Reports* journals.

Author contributions

H.K., C.P. and S.P. conceived the idea for this work. T.O., H.K. and H. L. fabricated the stretchable conductor and conducted related electrical and mechanical experiments. Y.J. confirmed the durability of the stretchable conductor through TEM analysis. M.S., G.H., J.K., and J.S. conducted experiments, including fabricating M-OIA samples and testing their adhesion. H.L. and C.P. developed a disease classification algorithm. T.K., H.J., C.H., I.L., J.C and J.K revised the manuscript. H.K., C. P. and S.P. oversaw the project, revised the manuscript, and led the effort to completion.

CRediT authorship contribution statement

Chanhyeok Park: Software, Formal analysis. **Hanbit Jin:** Writing – review & editing. **Taeyeon Oh:** Visualization, Validation, Methodology, Investigation, Formal analysis. **Jihun Son:** Formal analysis. **Sungjun Park:** Writing – review & editing, Writing – original draft, Visualization, Project administration, Methodology, Investigation, Conceptualization. **Alexander Tipan-Quishpe:** Validation. **Yong-Ryun Jo:** Formal analysis. **Myung-Han Yoon:** Validation. **Tae-Wook Kim:** Writing – review & editing. **Hye Jin Kim:** Writing – review & editing, Writing – original draft, Visualization, Methodology, Investigation, Conceptualization. **Gui Won Hwang:** Formal analysis. **Changhyun Pang:** Writing – review & editing, Writing – original draft, Visualization, Methodology, Investigation, Conceptualization. **Jinhyung Kim:** Formal analysis. **Chan-**

Hwa Hong: Writing – review & editing. **Minwoo Song:** Visualization, Validation, Methodology, Investigation, Formal analysis. **Inho Lee:** Writing – review & editing. **Hyunkeun Lee:** Visualization, Validation, Methodology, Investigation, Formal analysis. **Jun-Gyu Choi:** Writing – review & editing. **Hansu Kim:** Formal analysis. **Ji Hwan Kim:** Writing – review & editing. **Hyeongbeom Lee:** Formal analysis.

Declaration of Competing Interest

The authors declare that they have no known competing financial interests or personal relationships that could have appeared to influence the work reported in this paper.

Acknowledgments

This research was supported by the Nano & Material Technology Development Program through the National Research Foundation of Korea (NRF) funded by Ministry of Science and ICT (Grant No. RS-2024-00403639). The authors gratefully acknowledge the support from the National Research Foundation of Korea (RS-2024-00352352). This work was supported by the Technology Innovation Program (Grant No. RS-2022-00154781) funded by the Ministry of Trade, Industry & Energy (MOTIE, Korea). This research was also supported by the MSIT, Korea, under the ITRC (Information Technology Research Center) support program (Grant No. IITP-2023-2020-0-01461) supervised by the IITP (Institute for Information & communications Technology Planning & Evaluation). This study was supported by Hyoung-Min Choi of Phonics Co., Ltd. for the development of the FPCB module, and by the IC Design Education Center (IDEC), Korea, for providing the EDA tool.

Appendix A. Supporting information

Supplementary data associated with this article can be found in the online version at [doi:10.1016/j.mser.2025.101059](https://doi.org/10.1016/j.mser.2025.101059).

Data availability

Data will be made available on request.

References

- [1] S. Niu, N. Matsuhisa, L. Beker, J. Li, S. Wang, J. Wang, Y. Jiang, X. Yan, Y. Yun, W. Burnett, A.S.Y. Poon, J.B.-H. Tok, X. Chen, Z. Bao, *Nat. Electron.* 2 (2019) 361–368.
- [2] M. Xia, J. Liu, B.J. Kim, Y. Gao, Y. Zhou, Y. Zhang, D. Cao, S. Zhao, Y. Li, J. Ahn, *Adv. Sci.* 11 (2024) 2304871.
- [3] R. Kaveh, C. Schwendeman, L. Pu, A.C. Arias, R. Muller, *Nat. Commun.* 15 (2024) 6520.
- [4] S.P. Lee, G. Ha, D.E. Wright, Y. Ma, E. Sen-Gupta, N.R. Haubrich, P.C. Branche, W. Li, G.L. Huppert, M. Johnson, H.B. Mutlu, K. Li, N. Sheth, J.A. Wright, Y. Huang, M. Mansour, J.A. Rogers, R. Ghaffari, *NPJ Digit. Med.* 1 (2018) 2.
- [5] P. Di, Y. Yuan, M. Xiao, Z. Xu, Y. Liu, C. Huang, G. Xu, L. Zhang, P. Wan, *Adv. Sci.* (2024) 2401800.
- [6] S. Sundrani, J. Chen, B.T. Jin, Z.S.H. Abad, P. Rajpurkar, D. Kim, *NPJ Digit. Med.* 6 (2023) 60.
- [7] T. Tat, A. Libanori, C. Au, A. Yau, J. Chen, *Biosens. Bioelectron.* 171 (2021) 112714.
- [8] G.-H. Lee, Y.R. Lee, H. Kim, D.A. Kwon, H. Kim, C. Yang, S.Q. Choi, S. Park, J.-W. Jeong, S. Park, *Nat. Commun.* 13 (2022) 2643.
- [9] S. Kee, N. Kim, H. Park, B.S. Kim, M.Y. Teo, S. Lee, J. Kim, K. Lee, *Macro Chem. Phys.* 221 (2020) 2000291.
- [10] Y. Wang, C. Zhu, R. Pfattner, H. Yan, L. Jin, S. Chen, F. Molina-Lopez, F. Lissel, J. Liu, N.I. Rabiah, Z. Chen, J.W. Chung, C. Linder, M.F. Toney, B. Murmann, Z. Bao, *Sci. Adv.* 3 (2017) e1602076.
- [11] S. Kim, J. Lee, W.G. Chung, Y.-M. Hong, W. Park, J.A. Lim, J.-U. Park, *ACS Nano* 18 (2024) 24364–24378.
- [12] T. Lim, H.J. Kim, S. Won, C.H. Kim, J. Yoo, J.H. Lee, K.S. Son, I.-W. Nam, K. Kim, S. Y. Yeo, B.J. Yeang, J.H. Kim, H. Zhang, S. Lee, *ACS Appl. Nano Mater.* 6 (2023) 8482–8494.
- [13] M. Amjadi, A. Pichitpajongkit, S. Lee, S. Ryu, I. Park, *ACS Nano* 8 (2014) 5154–5163.

- [14] S. Jeong, S. Heo, M. Kang, H.-J. Kim, *Mater. Des.* 196 (2020) 109178.
- [15] L. Zhang, K.S. Kumar, H. He, C.J. Cai, X. He, H. Gao, S. Yue, C. Li, R.C.-S. Seet, H. Ren, J. Ouyang, *Nat. Commun.* 11 (2020) 4683.
- [16] A. Kihara, *Prog. Lipid Res.* 63 (2016) 50–69.
- [17] M.D. Dickey, R.C. Chiechi, R.J. Larsen, E.A. Weiss, D.A. Weitz, G.M. Whitesides, *Adv. Funct. Mater.* 18 (2008) 1097–1104.
- [18] F. Li, Y. Hu, W. Han, Y. Fu, M. Li, C. Li, C. Hu, *Phys. Fluids* 34 (2022) 114118.
- [19] T. Otsuki, N. Manyuan, H. Kawasaki, *Mater. Chem. Phys.* 314 (2024) 128844.
- [20] J. Wu, J. Hu, Y. Feng, H. Fan, K. Wang, Z. Deng, *Chem. Eng. J.* 458 (2023) 141400.
- [21] H. Huang, J. Shen, S. Wan, L. Han, G. Dou, L. Sun, *ACS Appl. Mater. Interfaces* 15 (2023) 11549–11562.
- [22] L. Liu, K. Kuffel, D.K. Scott, G. Constantinescu, H.-J. Chung, J. Rieger, *Biomed. Phys. Eng. Express* 4 (2017) 015004.
- [23] D.Alemu Mengistie, P.-C. Wang, C.-W. Chu, *J. Mater. Chem. A* 1 (2013) 9907.
- [24] P. Li, K. Sun, J. Ouyang, *ACS Appl. Mater. Interfaces* 7 (2015) 18415–18423.
- [25] Z. Wang, J. Zhang, J. Liu, S. Hao, H. Song, J. Zhang, *ACS Appl. Mater. Interfaces* 13 (2021) 5614–5624.
- [26] N. Matsuhisa, D. Inoue, P. Zalar, H. Jin, Y. Matsuba, A. Itoh, T. Yokota, D. Hashizume, T. Someya, *Nat. Mater.* 16 (2017) 834–840.
- [27] C. Liu, P. Wang, J. Hu, S. Cheng, S. Pan, P. Xu, Y. Ding, *Synth. Met.* 256 (2019) 116140.
- [28] E. Dazou, Y. Lin, H. Faber, E. Yengel, X. Sallenave, C. Plesse, F. Goubard, A. Amassian, T.D. Anthopoulos, *Adv. Funct. Mater.* 30 (2020) 2001251.
- [29] L. Flandin, Y. Bréchet, J.-Y. Cavallé, *Compos. Sci. Technol.* 61 (2001) 895–901.
- [30] S. Baik, D.W. Kim, Y. Park, T.-J. Lee, S. Ho Bhang, C. Pang, *Nature* 546 (2017) 396–400.
- [31] J. Lee, G.W. Hwang, B.S. Lee, N.-J. Park, S.-N. Kim, D. Lim, D.W. Kim, Y.S. Lee, H.-K. Park, S. Kim, J.W. Kim, G.-R. Yi, K.H. Kim, C. Pang, *ACS Nano* (2024) acsnano.3c09304.
- [32] D.W. Kim, K. Song, D. Seong, Y.S. Lee, S. Baik, J.H. Song, H.J. Lee, D. Son, C. Pang, *Adv. Mater.* 34 (2022) 2105338.
- [33] J.-H. Choi, Y.-R. Jeoung, I. Kim, J.-H. Chang, *Interspeech 2024 (in:)*, ISCA, 2024, pp. 3749–3753 (in:).
- [34] S. Srivastava, P. Kumar, V. Chaudhry, A. Singh, *SN Comput. Sci.* 1 (2020) 81.



Dr. Hye Jin Kim is a Senior Research Engineer in the Department of Intelligent Components and Sensors Research Section at Electronic and Telecommunications Research Institute (ETRI) and the Department of Advanced Device Technology at the University of Science and Technology, Republic of Korea. Dr. Kim's research focuses on stretchable electronics, physical and haptic sensors and wearable healthcare soft electronics.



Prof. Changhyun Pang is currently conducting independent research as a full professor in the School of Chemical Engineering at Sungkyunkwan University (SKKU). He is also an adjunct professor at Samsung Advanced Institute for Health Science & Technology (SAIHST) at Samsung Medical Center. His research interests are in super-intelligent bioinspired polymer 3D-architecture for (i) dry/wet adhesion, (ii) biomedical and bioelectronics interface, and (iii) smart soft robotics and XR haptic interfaces. During his career, he is selected as a member of Young Korean Academy of Science and Technology (Y-KAST), and has awarded several prestigious awards, including the Science and Technology Award from the Korean government and the Outstanding Polymer Young Scientist Award from the Korean Society of Polymers.



Prof. Sungjun Park is an Associate Professor in the Department of Electrical and Computer Engineering and the Department of Intelligence Semiconductor Engineering at Ajou University, Republic of Korea. He earned his PhD in 2016 from the School of Materials Science and Engineering at the Gwangju Institute of Science and Technology, Republic of Korea. Before joining Ajou University in 2020, he conducted postdoctoral research at RIKEN in Japan and worked as a Senior Researcher at the Samsung Advanced Institute of Technology (SAIT) in the Republic of Korea. Prof. Park's research focuses on skin-conformal electronic materials, devices, and integration for wearable sensors and bioelectronics.